FULL PAPER

Defect chemistry, electrical properties and evaluation of new oxides Sr₂CoNb₁₋ₓTiₓO₆₋δ (0≤x≤1) as cathode materials for Solid Oxide Fuel Cells

M. Teresa Azcondo*,[a], Mercedes Yuste[a], Juan Carlos Pérez-Flores[a], Daniel Muñoz-Gil[b], Susana García-Martín[b], Alvaro Muñoz-Noval[c], Inés Puente Orench[d], Flaviano García-Alvarado[a] and Ulises Amador*,[a]

Abstract: The perovskite series $Sr_2CoNb_{1-x}Ti_xO_{6-\delta}$ (0≤x≤1) is investigated in the full compositional range to assess its potential as cathode material for solid state fuel cell (SOFC). The variation of transport properties and thus, the area specific resistances (ASR) are explained by a detailed investigation of the defect chemistry. Increasing titanium content from x=0 to x=1 produces both oxidation of Co^{3+} to Co^{4+} (from 0% up to 40%) and oxygen vacancies (from 6.0 to 5.7 oxygen atom/formula unit) though each charge compensation mechanism predominates in different compositional ranges. Neutron diffraction reveals that samples with high Ti-contents lose a significant amount of oxygen on heating above 600K. Oxygen is partially recovered on cooling since the oxygen release and uptake show noticeably different kinetics. The complex defect chemistry of these compounds, together with the compositional changes upon heating-cooling cycles and atmospheres produce, a complicated behaviour of electrical conductivity. Cathodes containing $Sr_2CoTiO_{6-\delta}$ display low ASR values, 0,13 Ωcm^2 at 973 K, comparable to those of the best compounds reported so far, being a very promising cathode material for SOFC.

Introduction

Perovskites are very versatile materials that have been proposed as components of several electrochemical devices as for example fuel cells, [1] electrolyzers[2] and oxygen transport membranes[3]. For the former not only cathodes but also anodes and even electrolytes based on perovskite-like compounds have been

[a] M. Teresa Azcondo*, Mercedes Yuste, Juan Carlos Pérez-Flores, Flaviano García-Alvarado and Ulises Amador*,
Departamento de Química y Bioquímica, Facultad de Farmacia, Universidad CEU San Pablo, E-28668, Boadilla del Monte, Madrid, Spain.
azcondo@ceu.es
uamador@ceu.es
[b] Daniel Muñoz-Gil, Susana García-Martín
Departamento de Química Inorgánica, Facultad Ciencias Químicas, Universidad Complutense, E-28040 Madrid, Spain.
[c] Alvaro Muñoz-Noval
Instituto de Ciencia de Materiales de Madrid-ICMM/CSIC, Madrid, Spain and SpLine Spanish CRG Beamline at the ESRF, Grenoble, France.
[d] Inés Puente Orench
Instituto de Ciencia de Materiales de Aragón, CSIC–Universidad de Zaragoza and Institut Laue-Langevin, CS20156, F-38042 Grenoble Cedex 9, France.

proposed and are considered presently the state-of-the art in such applications[4]. Accommodation of cations of different size in different crystallographic sites produce structural distortions to lower symmetries when compared to the arystotype $SrTiO_3$ whereas different charges of these cations give rise to a variety of electrical and electrochemical properties. Moreover, perovskites show a quite flexible microstructure that influences also their properties[5] including transport properties, as oxygen conductivity, and electrochemical activity.[6]

Among perovskites, those called "double perovskites" with general formula $A_2BB'O_6$ present a variety of compositions and properties, related to the capability of the simple perovskite structure to accommodate different transition metal cations B and B' of different sizes and electronic structures. Besides, partial substitution of cations in the A-site opens new possibilities, including the induction of anionic vacancies through aliovalent substitution. The most investigated cathode material, $La_{1-x}Sr_xMnO_3$ (LSM), is obtained by substitution of La^{3+} by Sr^{2+}. Aliovalent substitution improves the electronic conductivity (due to small polarons hopping related to the manganese mixed oxidation state, Mn^{3+}/Mn^{4+}) with respect to the parent $LaMnO_3$.

We have recently studied $La_{2-x}Sr_xCoTiO_6$ [7] (0≤x<1) and $La_{2-x}CoTiO_{6-\delta}$ (0.05 <x <0.20)[8] series. In the former, La/Sr replacement produces a significant increase of electronic conductivity (from 3.6 10^{-2} Scm⁻¹ for the parent compound to 1.4 S cm⁻¹ for x = 0.4),[8] in as much as the sole charge compensation mechanism is the oxidation of Co^{2+} to Co^{3+}. La-deficiency is compensated through two main mechanisms: the oxidation of Co^{2+} to Co^{3+} on one hand, which is predominant at low x and creation of oxygen vacancies that predominates at intermediate x. At high x values both are operating. The existence of the two extrinsic defects, Co^{3+} and oxygen vacancies, explains the variation of the total electrical conductivity with oxygen partial pressure.

There is other related double perovskite $Sr_2CoNbO_{6-\delta}$, where the operating redox couple to tune electrical properties may be based on Co^{3+}/Co^{4+} instead of Co^{2+}/Co^{3+} and still the reports on their possible applications are scarce[9] . In addition, some structural characteristics have been already reported.[10] Our own studies on this interesting double perovskite started with the investigation of the structure, microstructure and magnetic properties of Ti-containing derivatives, $Sr_2CoNb_{1-x}Ti_xO_{6-\delta}$ (0≤x≤0.5)[5]. These materials present a complex microstructure consisting of domains a double-cubic-perovskite grown in a simple-cubic perovskite matrix. The size and the number of domains of double-perovskite

(with rock salt ordering of the B-ions) depend on the degree of substitution of Nb^{5+} by Ti^{4+}. Note that it is well established that not only structure but also microstructure have a strong influence on the electrical properties.[11] Aliovalent substitution of Nb^{5+} by Ti^{4+} produces the oxidation of Co^{3+} to Co^{4+} for low x values whereas a second mechanism, creation of oxygen vacancies, starts to operate at high x values.[5] Thus, change of Co^{3+}/Co^{4+} ratio as well as oxygen content with x may have a significant effect on both electrical and electrochemical properties of the title compounds. Therefore, here we report on potential use of $Sr_2CoNb_{1-x}Ti_xO_{6-\delta}$ (0 ≤ x ≤ 1) series compounds as SOFC electrode. Note that besides mixed oxidation state and oxygen vacancies the presence of small amounts of titanium may enhance catalytic effect for oxygen reduction improving their electrochemical performances.

Results and Discussion

Compositional and structural characterization

As determined by XRD and EDS, all the as-prepared samples $Sr_2CoNb_{1-x}Ti_xO_{6-\delta}$ (0≤x≤1.0) are single phase. Within the experimental errors, their chemical compositions match with the nominal ones; even more, the distribution of all the constituting elements was confirmed to be homogeneous throughout the samples. Back-scattered electron (BSE) images and the corresponding element-distribution maps for different compositions are shown in Figs. SI 1 to SI 3. Therefore, the Ti^{4+} substitution by Nb^{5+} ions can be considered effective and homogeneous for all the samples.

Recently, J. Bashir and K. Shaheen[9b] reported a structural model of tetragonal symmetry for $Sr_2CoNbTiO_{6-\delta}$ (S.G. I4/m). However, in a recent paper using XRD and NPD data, we report a different average structure of oxides $Sr_2CoNb_{1-x}Ti_xO_{6-\delta}$ (0 ≤ x ≤ 0.5). It can be described as a simple cubic perovskite (S.G. Pm-3m) with Sr located in 1b (½ ½ ½), Co/Nb/Ti randomly distributed in the 1a (0 0 0) and oxygen in 3d (½ 0 0) sites.[5] The fitting of the XRD data revealed that the rest of the series members (i.e. those with 0.5 < x ≤ 1.0) also present the ideal perovskite structure with no cationic ordering or octahedral tilting, in agreement with the tolerance factors close to one, which ranges from 0.989 to 1.010 (see Fig. SI 4 to SI 13).

On the other hand, as Figure 1 shows, the lattice parameter presents an interesting dependence with titanium content.

Figure 1. **Lattice parameter (blue squares), oxygen content per f.u. (green diamonds) and Co^{4+} content (red circles), both obtained by TGA and redox titration, as a function of the level of aliovalent substitution Nb^{5+} by Ti^{4+}.**

For low degree of aliovalent substitution (c.a. 10%) the cell expands, whereas from x > 0.1 it continuously contracts. This latter is the expected behaviour considering both, the sizes of Nb^{5+} (0.64 Å) and Ti^{4+} (0.605) and the effect of the aliovalent substitution of Nb^{5+} by Ti^{4+} on the oxidation state of cobalt. In fact, two charge-compensating mechanisms operate because of this substitution: the oxidation of Co^{3+} (^{HS}r= 0.61 Å, ^{LS}r 0.545 Å) to Co^{4+} (^{HS}r=0.53 Å) which contributes to a cell contraction as well; and the creation of oxygen vacancies, which would induce a volume expansion due to the loss of Madelung energy. It is obvious from

Fig. 1 that in the present materials the size effect due to cobalt oxidation is the predominant one. In this connection, Rietveld analysis of the XRD patterns shown in Figs. SI4 to SI13 suggests the existence of some amount of oxygen vacancies that increases as the degree of aliovalent substitution does. However, X-ray diffraction is not the best technique to deal with structural features associated with light atoms such as oxygen; therefore, other complementary techniques have been used to quantify the oxygen stoichiometry of the title oxides. Using redox titration and TG analyses independently we confirmed the dependence of oxygen content on the degree of substitution; the results are plotted in Figure 1.

The volume expansion for low levels of substitution may be associated to the evolution of the microstructure. Recently[5] we found that the $Sr_2CoNb_{1-x}Ti_xO_{6-\delta}$ oxides present a flexible microstructure which evolves with the Ti/Nb ratio. The parent material (x=0) present domains of cubic double perovskite with rock-salt order on the B-sites grown in a matrix of cubic simple disordered material. As Nb is substituted by Ti, the size and number of domains with double perovskite structure decrease, resulting in the increase of metal-metal repulsions since interactions between highly charged Nb^{5+} ions are more probable in the disordered perovskite in comparison with the ordered structure. Besides, a complex microstructure consisting of intergrowth of small domains will provide a mechanism to accommodate a large amount of anion vacancies (as those observed in Figure 1) in the domain walls.

Evolution of the structure and composition with temperature

The understanding of the electrical and electrochemical properties of a SOFC material requires the knowledge of its structure at operational temperatures as well as its thermal evolution, including thermal expansion. Besides, oxygen loss could occur, which may be relevant for the electrochemical properties. Thus, a representative sample of the series, $Sr_2CoNb_{0.10}Ti_{0.90}O_{6-\delta}$ (the same batch used in the XAS experiments) was studied by NPD at different temperatures from RT to 1173 K. To avoid the effect of high vacuum used in the furnace, the powder sample was wrapped with a platinum foil and introduced into a sealed quartz ampoule filled with air. Figure 2 shows the graphic result of the fitting of the NPD pattern recorded at RT and 1173 K to a cubic simple perovskite structural model. This structure is kept within the whole temperature range, the only varying parameters being the unit cell size and the oxygen content; the thermal evolution of both parameters is depicted in figure 3.

Figure 2. Experimental (red circles) and calculated (black continuous line) NPD patterns (and their difference, blue line at the bottom) for $Sr_2CoNb_{0.10}Ti_{0.90}O_{6-\delta}$ at RT (a) and 1173 K (b). The vertical bars indicate the Bragg peaks of the perovskite oxide (first row) and Pt foil (second row).

At room temperature anion deficiency is detected since the oxygen content is 5.75, corresponding to δ=0.25 and to 40% of Co^{4+}, which nicely agrees with the results obtained by redox titration (Figure 1) and XAS (see below). Oxygen release starts around 450 K and continues up to 1173 K. On cooling, oxygen is partially recovered, but only at quite low temperature. In fact, the material remains highly deficient almost down to RT; this may be due to kinetic reasons since along the thermodiffraction experiment the sample is, undoubtedly, far from equilibrium. In any case, the oxygen loss influences the electrical and electrochemical properties, as observed in other 3d-metal containing oxides, in as much as it induces changes of the oxidation state of metal ions.[12]

Figure 3. Thermal evolution of the oxygen content per f.u. and unit cell volume for $Sr_2CoNb_{0.10}Ti_{0.90}O_{6-\delta}$ as obtained from NPD.

On the other hand, the linear thermal expansion coefficient (TEC) for $Sr_2CoNb_{0.10}Ti_{0.90}O_{6-\delta}$ in the 600 to 1100 K temperature range is α_L= 21.4(3) 10^{-6} K^{-1}. This quite high value, when compared to that of the electrolyte CGO (α_L= 9.5(3) 10^{-6} K^{-1}) [13], may be associated to the oxygen loss. To confirm this hypothesis we have performed two kinds of experiments:

a) XRD patterns of the x=0.9 oxide have been collected during two heating-cooling cycles in a continuously evacuated chamber (this avoids re-oxidation and consequently the second heating cycle was performed on a reduced sample);

b) the TEC for the $Sr_2CoNb_{0.9}Ti_{0.1}O_{6-\delta}$ member of the series, which present cobalt in low oxidation state and experiences much lower oxygen loss, has been determined.

The TEC determined for $Sr_2CoNb_{0.10}Ti_{0.90}O_{6-\delta}$ in the first and second heating steps are similar and very close to that determined by NPD (see Fig. SI 14); even more, the value obtained after reduction (second cycle) is slightly higher than that of the pristine material. This suggests that the large cell expansion of these oxides is not related to oxygen release. This is confirmed by the behaviour of $Sr_2CoNb_{0.9}Ti_{0.1}O_{6-\delta}$ (Fig. SI 15), whose oxygen loss is negligible but its TEC is even higher than that of the x=0.9 oxide (the corresponding values are α_V= 64.3(1) 10^{-6} K^{-1} for the latter and α_V= 67.8(1) 10^{-6} K^{-1} for the former). It is reported in the literature that high values of TEC are intrinsic to cobaltites as it is due to a spin transition of Co^{3+} [4b, 14]; thus, the higher the content of trivalent cobalt the higher the TEC. Our results totally agree with this hypothesis.

Cobalt oxidation state

As discussed in previous sections, for $Sr_2CoNb_{1-x}Ti_xO_{6-\delta}$ oxides the concentration of oxygen vacancies continuously increases with x in the range 0 ≤ δ ≤ 0.30 (Fig. 1). But the evolution of the cobalt oxidation states is slightly different: for low Ti-contents (0 ≤ x ≤ 0.20) the decreasing of positive charge due to replacement of Nb^{5+} by Ti^{4+} is mainly compensated by oxidation of Co^{3+} into Co^{4+} and therefore very few oxygen vacancies are created. In the compositional range 0.30 ≤ x ≤ 0.50, cobalt oxidation state remains constant to ca. 15% of tetravalent cobalt while the concentration of oxygen vacancies noticeably increases (0.05 ≤ δ ≤ 0.17). From x = 0.6 to x = 0.90 oxidation of cobalt dominates again as the charge compensating mechanism, though anion substoichiometry keeps increasing (0.18 ≤ δ ≤ 0.25). At x = 0.90 the amount of Co^{4+} reaches a maximum of 40% and the same value is observed for the end member of the series x = 1.00 which shows the highest amount of oxygen vacancies (δ ≈ 0.30).

Large amounts of oxygen vacancies and cobalt in average (mixed) high oxidation state (Co^{3+} and Co^{4+}) may result in high ionic and electronic conductivities, both desirable properties in a SOFC cathode material. Worth to note, the title perovskites lose oxygen on heating in air. This being more pronounced for those members of the series with cobalt in higher nominal oxidation state, i.e. with high degree of aliovalent substitution, see Fig. 3 for the x=0.9 member. This could be a drawback for real applications since decreasing of p-charge carriers and mechanical stress could be induced by long-term exposure under operational conditions.

A sample of composition $Sr_2CoNb_{0.10}Ti_{0.90}O_{6-\delta}$, with a high degree of aliovalent substitution, was studied by XAFS. Figure 4a shows the Co K-edge spectra of this material together with the corresponding references for metallic Co and some relevant oxides. Clear shift in the edge position and differences in the edge shape is observed even by eye inspection. The variations in the electronic structure of Co are tightly related to the local environment and the X-ray absorption near to edge spectrum (XANES) shape is highly sensitive to subtle differences in the scattering atom environment, both structural and electronic. According to the Kunzl's rule, the edge shift from the metallic state reference (with oxidation state nominally zero) is roughly proportional to the oxidation state in transition metal oxides. [15] In order to give a reliable and quantitative estimation of the oxidation state of cobalt in the sample, for a precise edge position determination, the XANES spectra has been fitted to a Boltzman sigmoidal function, as successfully applied in previous works [16]:

$$y(\text{norm. absorbance}) = \frac{A_1 - A_2}{1 + \exp\left(\frac{(E - E_0)}{E_d}\right)} \quad (1)$$

where E_0 is the edge position, E_d is the curve slope at the edge and A_1 and A_2 are the extreme values of the sigmoidal function (respectively 1 and 0 in the usual XAS normalized spectrum). Attending to this calculation, we have obtained an accurate value for the cobalt formal oxidation state of +3.4 for this highly Ti-substituted material (i.e. x=0.90). This value can be interpreted, considering a bimodal population of Co(III) and Co(IV) cations, with 40% of tetravalent cobalt, which is in good agreement with the results obtained by chemical titration and TG analysis (Fig. 1), as well as by NPD (Fig. 3).

Regarding the shape of the spectra, we noticed a high intensity pre-peak feature, which in the K-edge of 3d metals is related to 1s-3d electric quadrupole transitions.[17] This transition is dipole forbidden and in principle weak for O_h symmetries in the 3d-transition elements (see, for instance, the cobalt oxides references here shown: metal coordination in CoO is O_h and in Co_3O_4 are both T_d and O_h). The pre-peak becomes more intense for tetrahedral symmetry as result of hybridization of the d-p orbital. Thus, in principle, the observed increase of the intensity can be assigned to a distortion of the local environment of Co, at least to a partial population of low symmetry sites in the structure. Another interesting feature is the double peak in the white line of the spectra (cusp of the edge or also known as main peak). This double peak is a very uncommon feature in oxides and is usually observed for fivefold coordination. [18] These evidences strongly

suggest a partial occupancy of Co in fivefold-coordinated sites (most probably as square pyramids).

To analyze the local structure of cobalt the average structural model obtained by NPD was used as starting point. Thus, we have considered an octahedral coordinated cation as a first approximation to model our experimental data. The fitting of the EXAFS spectrum in the real space is shown in Fig. 4b. Due to the complexity of the structure and considering we are only interested in the information from the first atomic shell, formed by oxygen anions, we have restricted our study to this range. Our calculations give average oxygen coordination in the first shell of 5.1(2) (86% of the fully occupied shell), suggesting a clearly anionic-deficient environment. This average coordination is compatible also with a partial population of cobalt in square pyramidal symmetry, in accordance with the double peak observed at the most intense maximum in the XANES spectrum and with our ab-initio calculations. It is a relevant result since suggests that the oxygen vacancies are mainly associated to cobalt ions, as corresponds to a metal which present a remarkable flexibility in both oxidation state and coordination number and geometry.[19] Considering the titration and TGA results, which give a composition of $Sr_2CoNb_{0.10}Ti_{0.90}O_{5.76}$ (δ = 0.24) there are two plausible arrangements to account for a so reduced coordination number of cobalt: the formation of cobalt clusters[20] associated to oxygen vacancies and the preferred accommodation of cobalt and vacancies in the large domains walls observed by TEM in these materials.[5]

On the other hand, the second shell, at c.a. 3.35 Å is formed by 8 Sr atoms and is clearly distinguished. This shell is structurally stable and in first approach is not expected to play an active role in the oxidation/reduction mechanism of these materials, though recent results revealed an important role of the perovskite A-site ions in the electrical properties of this sort of materials. [21]

Figure 4. XAS measurements of $Sr_2CoNb_{0.1}Ti_{0.9}O_{6-\delta}$ (a) XANES spectra of the pristine sample with corresponding references of Co and selected Co oxides and (b) module of the Fourier transform of the EXAFS spectrum of $Sr_2CoNb_{0.1}Ti_{0.9}O_{6-\delta}$ with the corresponding fit of the first coordination shell (Co-O).

Stability at different pO$_2$ and compatibility with electrolyte materials

FULL PAPER

The use of a given material as SOFC electrode depends on both its stability under operational conditions and on the chemical compatibility with the electrolyte. Since the title compounds are prepared in air their stability under oxidizing atmosphere is evident; it is worth to note that oxides $Sr_2CoNb_{1-x}Ti_xO_{6-\delta}$ with low Ti-content ($0 \leq x \leq 0.2$) are unstable under reducing conditions ($pO_2 \approx 10^{-21}$ atm,) (see Fig SI 16 and SI 17) contrary to what previously reported.[22] Although no so evident, members with high level of aliovalent substitution are also unstable upon reduction, as the XAS spectrum shown in Fig. SI 18 demonstrates for a sample of composition $Sr_2CoNb_{0.10}Ti_{0.90}O_{6-\delta}$.

Chemical compatibility with YSZ and CGO, commonly used as electrolytes, has been also checked. Oxides of the $Sr_2CoNb_{1-x}Ti_xO_{6-\delta}$ series present severe compatibility problems with YSZ under oxidizing atmosphere since they react (even under mild conditions: 1173K/15 hours/air) to yield large amounts of $SrZrO_3$ (see Fig. SI 19a). The extension of this reaction (i.e. the amount of $SrZrO_3$ produced) increases with x. On the contrary, the whole series is chemically compatible with CGO; Fig. SI 19b does not show any reaction product after the same experimental conditions above mentioned.

Therefore, conductivity measurements were performed in either air or pure oxygen, and polarization measurements on symmetric cells were conducted in air using CGO as electrolyte.

Electrical and electrochemical characterization dc-conductivity

Temperature dependence of conductivity measured by dc four-probe technique (σ_{dc}) for $Sr_2CoNb_{1-x}Ti_xO_{6-\delta}$ ($0 \leq x \leq 1$) in the 1173 – 350 K is depicted as an Arrhenius plot in Fig. 5. All the samples are *p*-type semiconductors, as demonstrates the increase of conductivity with temperature and its enhancement in pure oxygen compared to that in air (Fig. 6); some deviations from this general behaviour will be clarified in what follows.

A small-polaron hopping mechanism has been proposed to operate in the parent compound $Sr_2CoNbO_{6-\delta}$.[22a] However, the thermal dependence of conductivity of the whole series is more complex. Conductivity changes for every composition according to different activation energies in different temperature ranges and at high temperature saturation is observed. Two different behaviours have been found depending on the compositional range, low or high Ti- content.

Figure 5. Arrhenius representation of the total dc-conductivity in air for the $Sr_2CoNb_{1-x}Ti_xO_{6-\delta}$ ($0 \leq x \leq 1$) series in air (measurements performed on cooling from 1173 K to RT, see text), (a) x ≤ 0.3 and (b) x ≥ 0.6.

For low Ti-contents and temperatures below 600 K, conductivity increases with the degree of substitution, (Fig. 5a). However, for temperatures higher than 600 K deviation from Arrhenius behaviour occurs and conductivity displays a non-clear dependence on Ti-content. The finding is similar for the high Ti-containing members of the series (x ≥ 0.6) at any temperature in the investigated range, (Fig. 5b). In these cases a maximum of conductivity is observed between 650 K and 750 K. These findings are most likely due to the complex defect chemistry and microstructure of these materials[5] which strongly affect their charge transport mechanism.[22a]

As it was shown in Fig.1, in the low Ti-content range, the main charge compensating mechanism of the aliovalent substitution is the oxidation of Co^{3+} to Co^{4+} that can be described through (Eq.2). However, some oxygen vacancies are also induced (Eq. 3), as confirmed by NPD and other techniques (see Fig. 3); indeed, this latter mechanism is more important for high values of x. Thus, progressive substitution of Nb^{5+} by Ti^{4+} induces the increase of *p*-type charge-carriers, which are dominant for these semiconducting materials. Therefore, accordingly to incremented extrinsic holes given by Eq. (2) conductivity at a given temperature below 600 K increases with x as observed in samples with low Ti-contents ($0 \leq x \leq 0.3$).
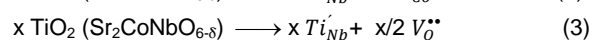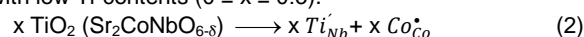
$$x\ TiO_2\ (Sr_2CoNbO_{6-\delta}) \longrightarrow x\ Ti'_{Nb} + x\ Co^{\bullet}_{Co} \qquad (2)$$

$$x\ TiO_2\ (Sr_2CoNbO_{6-\delta}) \longrightarrow x\ Ti'_{Nb} + x/2\ V^{\bullet\bullet}_O \qquad (3)$$

**Figure 6.** dc-conductivity on cooling under air (open black symbols) or pure oxygen (solid red symbols) for $Sr_2CoNb_{0.9}Ti_{0.1}O_{6-\delta}$ (circles) and $Sr_2CoNb_{0.1}Ti_{0.9}O_{6-\delta}$ (stars).

The sample with x= 0.3 deserves some comments. It follows the general behaviour up to 600 K, but above a deviation from steady conductivity increasing occurs and conductivities smaller than expected are observed. This is revealing the activation of a second process that tends to decrease number of charge carriers. One possibility is that above that temperature oxygen loss occurs in a significant extent producing *n*-type charge accordingly to Eq. (4) that annihilates *p*-type carriers Eq. (5):

$$O_O^x \longrightarrow \tfrac{1}{2}O_2 + V_O^{\bullet\bullet} + 2\,e^{'} \qquad (4)$$
$$p + n = null \qquad (5)$$
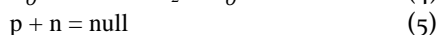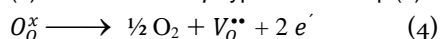
Expressed in a localized formalism electrons are trapped by Co^{4+} that is reduced to Co^{3+}:

$$2\,Co_{Co}^{\bullet} + O_O^x \longrightarrow 2\,Co_{Co}^x + V_O^{\bullet\bullet} + \tfrac{1}{2}O_2 \qquad (6)$$
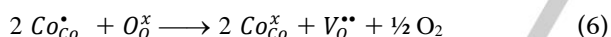
Thus, above 600 K thermal activation of remaining holes does not compensate the reduction of *p*-type charge carriers upon oxygen loss and conductivity tends to reach a constant value.

The *p*-type electronic conduction in the parent material $Sr_2CoNbO_{6-\delta}$ has been proposed to proceed via direct exchange among neighboring B-cations (Co and Nb) with incomplete d-shells.[22a] In a cubic disordered perovskite such as the title compounds, two paths for holes hopping are possible; those indicated as P1 and P2 in Fig. 7. The distance between the two 3d-cations is directly related to the difficulty of holes exchange and inversely to the probability of a single jump. Obviously P1 provides a better conduction path than P2, since the distance between adjacent B-ions are a_p and $2^{\frac{1}{2}}\,a_p$ (a_p refers to the cubic perovskite unit cell), respectively. It is also obvious than any structural or electronic effect hindering holes motion will result in a decrease of conductivity. Among the latter ones, any pathway involving Nb or Ti ions will be blocked since Nb^{5+} and Ti^{4+} can hardly be oxidized accepting a hole, to participate in charge transfer, as observed in other hole-conducting materials.[23] As stated above, the title materials present a complex microstructure, likely including cobalt clustering, which may affect the transport properties. Therefore, these aspects will condition the mobility of charge carriers, and together with its concentration will determine the conductivity at each temperature.

Figure 7. Schematic diagram of the conduction paths (P1 and P2) for small polarons hopping in $Sr_2CoNb_{1-x}Ti_xO_{6-\delta}$: small red balls represent oxygen atoms, blue spheres correspond to Co, Nb and Ti randomly distributes throughout B-sites and large green one represent Sr in A-sites.

The thermal evolution of conductivity for samples with high Ti-content is depicted in Fig. 5b. Materials with x= 0.6 and 0.7 present a behaviour somewhat similar to that observed for x=0.3 with a change of conductivity regime at high temperature and a clear tendency to reach saturation. However, for x = 0.8, 0.9 and 1.0 a maximum of conductivity arises at a temperature for which oxygen release is significant (between 600 K and 700 K, see Fig. 3 for the sample with x=0.9); above the maximum, conductivity clearly declines up to 900 K to start rising at temperatures higher than this (see Figs. 5b and 6). The data presented in Fig. 6 suggest that this behaviour is again related to the release of oxygen. Thus, dc-conductivity of the sample with x=0.9 (as a representative example) measured in pure oxygen reaches saturation but it does not clearly rise at high temperature as it does when treated under air. Besides, at high temperature the conductivity is lower in oxygen than in air. This can be explained as follow.

Above 900 K oxygen loss still occurs and originates electrons according to Eq. (4) in such a way that, once holes have been annihilated, the extra electrons induce *n*-type conduction. Both concentration and mobility of these *n*-type charge-carriers are thermally activated; as a result, conductivity rises on heating.

Total annihilation of holes according to Eq. (6) implies that all cobalt ions are trivalent and the oxygen content must be lower that the value determined by electroneutrality to allow some extra *n*-type charge carriers in the material or in a localized approach, some cation (Nb^{5+}, Ti^{4+} or Co^{3+}) must be reduced. In Fig. 3 it can be seen that the oxygen content at 1173 K is ca. 5.48 which is clearly below 5.55 that corresponds to total annihilation of holes. From the different electrical behaviour of samples with low Ti-content (low Co^{4+} content) and sample with high Ti- content (high Co^{4+} content) it seems that oxygen evolution is facilitated by high Co^{4+} concentration which is easily reducible. Thus, most likely at high temperature some Co^{2+} is formed rather than Ti^{3+} or Nb^{4+} according to Eq. (7)

$$2\,Co_{Co}^x + O_O^x \longrightarrow 2\,Co_{Co}^{'} + V_O^{\bullet\bullet} + \tfrac{1}{2}O_2 \qquad (7)$$
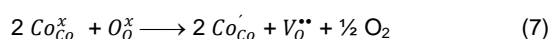
Some ionic conductivity might exist in these materials since they present large amount of oxygen vacancies; however, its

contribution to total conductivity is negligible when compared to electronic contribution.

The temperature of the conductivity maximum observed for x= 0.8, 0.9 and 1.0 is not likely to depend only on thermodynamic aspects given by action mass law as for examples those of equations (6) and (7) but also on kinetics aspects of oxi-reduction of metals and oxygen intake or releasing. To stress the influence of this aspect we come back to data on Fig. 3, which besides the thermal evolution of oxygen content on heating, shows additional data on cooling. Although data on cooling are limited, they clearly demonstrate that oxygen gain on cooling doesn´t follow a steady variation contrary to what observed for oxygen loss on heating. However, the oxygen content at room temperature after one complete heating- cooling cycle is similar to that of the pristine material. Once the sample is heated up to 1173 K and a noticeable amount of oxygen is lost, the material remains under-stoichiometric down to a temperature as low as 600 K; below this temperature the material is re-oxidized to reach oxygen content close to the original one. This behaviour is most likely due to kinetics aspects and evidences that in these materials oxidation-reduction reactions may be slow and this could have some influence on conductivity measurements.

The effect on conductivity of oxygen partial pressure and thermal history has been studied for two samples with high and low Ti-contents, $Sr_2CoNb_{1-x}Ti_xO_{6-\delta}$ (x = 0.1 and 0.9). Figure 8a shows that for the sample with lower Ti-content, $Sr_2CoNb_{0.9}Ti_{0.1}O_{6-\delta}$, there are not major differences regardless of whether the measurements are performed on either heating or cooling, either in oxygen or in air. In the low temperature range (up to 750 K approximately) conductivities are almost the same in air or oxygen atmospheres. However, at higher temperatures conductivities are slightly higher under oxygen, as correspond to a p-type semiconductor.

On the other hand, the conductivity of the oxide $Sr_2CoNb_{0.1}Ti_{0.9}O_{6-\delta}$ presents hysteresis on heating-cooling cycles in air (Fig. 8b), confirming the different kinetics of oxidation and reduction processes observed by NPD. Hysteresis diminishes at higher oxygen partial pressure, since oxygen loss/gain plays a crucial role in the red-ox behaviour of these materials. Regarding the dependence of conductivity at a given temperature with oxygen partial pressure, two regimes are observed: in the low temperature region conductivity increases with oxygen partial pressure, in full agreement with p-type semiconducting behaviour displayed by the entire series. However, above the maximum, when holes have been annihilated (Eq. (6)) and n-type carriers (Eq. (7)) dominates, electrical conductivity is higher in air, which is a less oxidant atmosphere than pure oxygen.

Transport properties are the result of at least two factors: the concentration and nature of charge-carries, and their mobility. In the title oxides, the former are related to the oxygen content given by Eq. (4-7); whereas the latter is related with conduction paths. The atmosphere and the thermal history can modify not only the oxygen content but also the microstructure, which has a strong influence on conduction paths. Thus, to draw a detailed explanation of the dependence of conductivity with temperature and pO$_2$ in these oxides is a difficult task.

Polarization tests on symmetrical cells

Figure 9 shows the ASR values determined from the impedance spectra in the range 823 – 973 K for composites made with oxides $Sr_2CoNb_{1-x}Ti_xO_{6-\delta}$ (x = 0, 0.1, 0.3, 0.5, 0.7 and 1.0) and CGO as previously described. Broadly speaking, the ASR values are lower for samples with increasing Ti-contents. Worth to note, for these materials ASR noticeably increases after being heated at 973 K, as we detected when measured on cooling from this

temperature. This is shown in Fig. 10 which compares the impedance spectra of $Sr_2CoNb_{0.5}Ti_{0.5}O_{6-\delta}$ and $Sr_2CoTiO_{6-\delta}$ in air at 923 K; the hysteresis observed in ASR may have an origin similar to that pointed for total conductivity (σ_{dc}), this is, the different kinetics of oxygen release and uptake (Figs. 3 and 8). Although we observe this behaviour in the whole temperature and for all the samples, this worsening of the cathode performance is more important for high Ti-contents. Anyhow, the ASR values at intermediate temperature (973 K) range from 0.12 to 0.82 Ω.cm² for x=0 and 1.0, respectively; whereas the activation energies are in the range 1.1 to 1.4 eV which are comparable to those of similar systems. [23-24]

Figure 8. (a) dc-conductivity on heating and cooling under air or pure oxygen for (a) of $Sr_2CoNb_{0.9}Ti_{0.1}O_{6.\delta}$ and (b) of $Sr_2CoNb_{0.1}Ti_{0.9}O_{6-\delta}$

In order to separate the different contributions of the electrochemical processes of the cell, the impedance spectra have been fitted to equivalent circuits. The simplest model giving good fits consists of: an inductance (L), due to the wires of the electrochemical cell and equipment, an ohmic resistance (Rs), mainly associated with the total ion transport in the electrolyte, and a number of parallel RQ-elements connected in series, associated to processes at the electrolyte-electrode interface and at the electrode surface (R=resistance, Q = constant phase element with impedance $Q^{-1}(i\omega)^{-n}$). [25]

Figure 9. Arrhenius plot of the area-specific resistance (ASR) values obtained from the impedance spectra of the $Sr_2CoNb_{1-x}Ti_xO_{6-\delta}$/CGO symmetrical cells on heating in air.

Figure 10. Nyquist plot (after substraction of the apparent electrolyte resistance and instrumental inductance) of the impedance spectra of symmetrical cells made using composites $Sr_2CoNb_xTi_{1-x}O_{6-\delta}$ (x=0.5 or 1.0):CGO (70:30% wt), measured at 923 K in air. Solid red symbols correspond to the first measurement (on heating from RT) and open blue symbols to that on cooling (after heated).

The Bode plot (dependence of the phase angle with frequency) provides useful information to determine the number of processes in complex systems such as composites or porous electrodes.[26] In Fig. 11 the Bode plot corresponding to composite electrode containing $Sr_2CoTiO_{6-\delta}$ revealed the presence of three processes at low, intermediate and high frequencies (denoted as LF, IF and HF, respectively); similar behaviour is observed for all samples.

Although the LF and IF processes tend to collapse on heating, at the highest temperature studied (973 K) they can still be separated.

Therefore, the equivalent circuit used to fit the IS spectra can be denoted as $LR_s(RQ)_{HF}(RQ)_{IF}(RQ)_{LF}$ and is shown in the inset of Fig. 12a. This Fig. 12 shows the fits of the IS spectra of $Sr_2CoTiO_{6-\delta}$ and $Sr_2CoNbO_{6-\delta}$, the initial and end members of the series, on heating and cooling at 873 K, to this equivalent circuit. For all the other cases the results are similar. The refined impedance parameters at different temperatures for these compounds on heating and cooling are given in Tables SI 1 to SI 4. The (RQ) values are related to the capacitance (C) and the relaxation frequency (f) (see Table 1), which can be calculated using expressions (8), (9) and (10).

$$C = \frac{(RQ)^{\frac{1}{n}}}{R} \quad (8) \qquad f = \frac{\omega}{2\pi} \quad (9) \quad \omega\,(RQ)^{-\frac{1}{n}} \quad (10)$$

Figure 11. Bode plot of the impedance spectra of symmetrical cells made using composites $Sr_2CoTiO_{6-\delta}$:CGO (70:30% wt), measured in air at different temperatures.

The capacitance and relaxation frequencies for the HF process are in the range of 0.001-1000 µFcm^{-2} and 100-0.01 MHz, respectively, which can be associated with oxide-ion transfer through the electrolyte-electrode interface.[25a, 27] Although as a general rule, the more vacancies there are, the faster oxygen can be absorbed by, and move through, the material and the material/electrolyte interface, higher electronic conduction also favors faster oxygen exchange. [25b] Since in the title materials these two features are opposite related with oxygen content (higher degree of vacancies results in lower electronic conductivity) the dependence of the HF process with Ti-content and oxygen vacancies concentration is not simple. In the heating cycle the resistance associated to this process seems to be related to the degree of aliovalent substitution, i.e. the value of x, in such a way that the higher the concentration of titanium the lower the resistance. This may be the result of both a higher ionic conductivity due to oxygen vacancies, created upon substitution of Nb^{5+} by Ti^{4+}, and a higher electronic conduction. [21] However, in the cooling cycle, once the samples lose some oxygen and the concentration of anionic vacancies has increased, the resistance and activation energies of this HF process slightly increase suggesting that the effect of a lower electronic conductivity is dominant (see Tables SI 1 to SI 4) since conductivity decreases upon reduction (Fig. 8).

At intermediate frequencies, IF process, the capacitance and relaxation frequency are between 10^{-2}-10^{-5} Fcm^{-2} and 10^1-10^2 Hz, respectively, which are both in the typical range for an electron charge transfer process.[22, 41] This process seems to be favored by a high electronic conductivity associated to samples with high degree of aliovalent substitution; thus the resistance corresponding this process is lower for highly substituted samples.

Finally, at low frequencies two main processes are usually observed: oxygen absorption/desorption associated with the reduction/oxidation reaction and diffusion. The latter case is characterized by n values smaller than 0.5; [28] in our cases the n-values are closer to 1, indicating a pseudo-capacitive behaviour.

The capacitances of the order of 10^{-1} Fcm^{-2} independently on temperature is similar to the chemical capacitance that arises as a consequence of a reduction process and formation of bulk oxygen vacancies in $(La_{0.6}Sr_{0.4})CoO_{3-\delta}$. [29] Besides, the relaxation frequencies in the range 10^{-1}-10 Hz support this assignment. Therefore, these materials experience some degree of reduction/oxidation on heating/cooling, respectively, as observed by NPD, much easier (lower resistance) for samples with higher Ti-contents. The capacitance is similar for all the samples since the microstructural and textural properties of the electrodes are the same as far as all of them have been prepared in the same manner and consequently the fraction of the cathode involved in the reaction is similar in all cases.

The contribution of these three processes to the ASR is somewhat different depending on the degree of aliovalent substitution and temperature. Thus, for x=0, $Sr_2CoNbO_{6-\delta}$, the resistances associated to the three processes are similar at all

temperatures (Tables SI 3 and SI 4) as none of them clearly dominates the resistive behaviour of the electrode. In other words, for x=0 the oxidation-reduction reaction, the electronic-charge transfer and the oxide-ion migration across the electrode/electrolyte interphase are similarly impeded. The ASR values determined for composite electrodes made of $Sr_2CoNbO_{6-\delta}$/CGO (70:30% wt) are pretty high limiting its use in real SOFCs. On the contrary, cathodes containing $Sr_2CoTiO_{6-\delta}$ display quite low ASR values at intermediate temperatures (Table SI 1 and SI 2). At 973 K an ASR value of 0.12 Ωcm^2 is similar to those of the best compounds reported so far: $SrNdCo_{0.75}Fe_{0.25}O_{4.08}$ and $SrNdCo_{0.75}Mn_{0.25}O_{4.08}$ (ca. 0.18 $\Omega.cm^2$ in both cases at 973 K)[30], and similar values at 1073 K for $La_4Ni_{2.6}Co_{0.4}O_{10+\delta}$ [31] and $NdSrCoO_{4+\delta}$.[32] The better performance of the x=1 member of the series is mainly due to higher conductivity which favors both electronic-charge transfer and oxidation-reduction processes.

A cross-sectional view of an electrode of composition $Sr_2CoNb_{0.7}Ti_{0.3}O_{6-\delta}$/CGO (70:30 wt %) after operation is presented in Fig. 13. A good adherence between the electrode composite and the electrolyte surface is observed. However, the electrode microstructure needs further optimization, since it consists of large particles (of micron size) of the active material covered by submicron particles of the electrolyte.

Figure 12. Impedance spectra, after subtraction of the apparent electrolyte resistance and instrumental inductance, of symmetrical cells made using composites $Sr_2CoNb_{1-x}Ti_xO_{6-\delta}$:CGO (70:30 %wt). IS spectra for $Sr_2CoTiO_{6-\delta}$ in air at 873 K in heating (a) and cooling cycles (b); (c) and (d) IS spectra for $Sr_2CoNbO_{6-\delta}$ in the same conditions in heating and cooling cycles, respectively. The spectra are fitted to the equivalent circuit represented in the inset of (a). The solid lines are the fitting results whereas small circles represent experimental data.

Figure 13. SEM micrograph of a cathode $Sr_2CoNb_{0.7}Ti_{0.3}O_{6-\delta}$/CGO (70:30 %wt) on CGO electrolyte after operation.

Conclusions

The perovskite series $Sr_2CoNb_{1-x}Ti_xO_{6-\delta}$ exhibits a cubic perovskite structure (S.G. Pm-3m) in the whole compositional range 0≤x≤1. The effect of temperature on the structure and composition is studied in the RT-1173K range which includes the SOFC operational temperature. A sample case, one with high titanium content, x=0.9, studied by NPD reveals a significant and reversible oxygen loss above 600 K. Thus in the pristine sample $Sr_2CoNb_{0.10}Ti_{0.90}O_{6-\delta}$ the oxygen content is 5.75 (δ=0.25 and 40% of Co^{4+}), which nicely agrees with the results obtained by redox titration and XAS. The sample loses oxygen continuously on heating and at 1173 K reaches an oxygen content of 5.48. The structure is kept up to 1173 K and after cooling, the lost oxygen is again gained. However, a different kinetics for both reduction and oxidation processes is observed. This sheds light on two other findings. First, the hysteresis observed in the behaviour of electrical conductivity upon cooling and heating cycle for samples with high titanium contents (high content of easily reducible Co^{4+}),

FULL PAPER

and secondly the hysteresis observed in ASR which is also larger for high titanium content samples.

Defect chemistry of this series involves two charge compensating mechanism as Ti-content increases. Increasing titanium content from x=0 to x=1 produces both oxidation of Co^{3+} to Co^{4+} (from 0% up to 40% Co^{4+}) and oxygen vacancies (from 6.0 to 5.7 oxygen atom/formula unit) though each charge compensation mechanism predominates in different compositional ranges. The complex defect chemistry of the title compounds together with the compositional changes upon heating/cooling cycles and atmospheres produce a very complicated behaviour of electrical conductivity that is explained satisfactorily. Thus, in the low Ti-content range progressive substitution of Nb^{5+} by Ti^{4+} induces the increase of p-type charge carriers and conductivity increases with x in the low temperature range (< 600 K). At higher temperature the effect of oxygen release, and the consequent sample reduction, is now evidenced as conductivity seems to level off because n-type charge carriers start to be formed annihilating p-type carriers. For the samples with high Ti-content, a maximum in conductivity evidences the competition between the two charge-carrier formation mechanisms. As result the thermally induced rise of conductivity due to the activation and motion of p-type carriers is counteracted, thus the conductivity is quite similar for all samples at operational temperatures. The important difference between low and high Ti-content samples is probably the amount of oxygen vacancies at operational temperatures that is higher in the latter, having a beneficial effect on ASR.

ASR values have been determined for composites of $Sr_2CoNb_{1-x}Ti_xO_{6-\delta}$/CGO (70:30% wt) in air assessing its potential use as cathode components. Broadly speaking, ASR values are lower for samples with high titanium content due to an increased amount of oxygen vacancies. For example ASR value at 973 K in air determined for composite electrodes made of $Sr_2CoNbO_{6-\delta}$:CGO (70:30% wt) is 0.82 Ωcm^2; such a high value limits its use in real SOFCs. On the contrary, cathodes containing $Sr_2CoTiO_{6-\delta}$ display in the same conditions, lower ASR values, 0.12 Ωcm^2, which are comparable to those of the best cathodes reported so far. Thus, some of the title oxides seem to be promising cathode materials for SOFC.

Experimental Section

The synthesis of these compounds has been carried out accordingly to previous reports by Azcondo et al.[5]

X-ray diffraction (XRD) patterns were recorded on a Bruker D8 high-resolution X-ray powder diffractometer, equipped with LynxEye fast detector, using monochromatic Cu($K\alpha$1) (λ= 1.5406 Å) radiation obtained with a germanium primary monochromator. Data were collected in the range 2θ = 10-150 (deg.) with a step width 0.015(deg.) (2θ) over a total exposure time period of 16 h. The powder diffraction data were analyzed by the Rietveld method, using the FullProf program.[33]

Neutron powder diffraction (NPD) experiments were performed at D1B instrument at Institute Laue Langevin (ILL, Grenoble, France), using a monochromatic beam of 1.2902 Å. The contribution of the instrument to the peaks width was determined by the instrument resolution function built from the experiment on $Na_2Ca_3Al_2F_{14}$ standard sample, whereas the wavelength was determined using a Si standard.

X-ray Absorption Spectroscopy (XAS) measurements were carried out at the Co K-edge (7709 eV) at the BM25A-Spline beamline in the European Synchrotron Radiation Facility (ESRF, Grenoble, France). The monochromator is a pseudo channel-cut type with a double Si(111) crystal type refrigerated at 200 K by a homemade ethanol cooling system. The

measurements were performed in fluorescence yield mode for the samples and at transmission mode for the references. Three scans were acquired for each sample in order to ensure reproducibility and to average the spectra and increase the signal to noise ratio. Both metallic Co and Co reference oxides references were measured in the same experimental conditions. Fluorescence signal was acquired with a 13-elements fluorescence detector SGX Sensortech. The XAS data were reduced applying standard procedures using the Demeter package[34] and fits on Extended X-ray Absorption Fine Structure (EXAFS) region for k3 weighted signals were carried out in r space using theoretical path functions calculated with FEFF8 code.[35]

Scanning electron microscopy (SEM) experiments were performed on sintered pellets using a FEI XL30® apparatus equipped with an EDAX® analyzer for energy dispersive spectroscopy (EDS). Metal composition was determined by analyzing several microcrystals of every sample (typically, ca. 20 microcrystals have been analyzed). Besides, these techniques have been used to determine the morphology and microstructure of the electrodes after electrochemical characterization.

The cobalt oxidation state (Co^{3+}/Co^{4+}) and oxygen content (assuming charge neutrality) of the samples were determined by thermogravimetric analysis using a D200 Cahn Balance under a reducing atmosphere and high temperature. For this purpose, typically ca. 70 mg of sample were weighed to a precision of ±0.0005 mg at a total reduced pressure of 400 mb containing 60% He:40% H_2 gas mixture to reach oxygen partial pressure (pO_2) of 10^{-28} atm. Afterwards, the sample was heated up to 1173 K (5 K min^{-1}). Moreover, independent determinations were performed by titration using potassium dichromate, as described in ref.[7]

The dc-conductivity (σ_{dc}) of the $Sr_2CoNb_{1-x}Ti_xO_{6-\delta}$ ($0 \leq x \leq 1$) compounds has been measured by the four probe technique on prismatic bars ($\approx$4.5 x 4 x 3 mm^3). Platinum wires and paste were used to ensure electrical contact. Measurements were performed in air in the temperature interval from 1173 to 350 K every 25 K; a value was recorded after stabilization of conductivity within a ±0.1% fluctuation in one hour. To determine the effect of the thermal history of the samples on conductivity, samples of composition $Sr_2CoNb_{1-x}Ti_xO_{6-\delta}$ (x=0.1 and 0.9) were measured under air and pure oxygen atmospheres on heating (from the lowest to the maximum temperature in the aforementioned range) and then on cooling. The chemical compatibility of the electrode materials $Sr_2CoNb_{1-x}Ti_xO_{6-\delta}$ (0≤x≤1) with powdered cerium gadolinium oxide, $Ce_{0.90}Gd_{0.10}O_{2-\delta}$, (CGO) (Fuel Cells Materials Corp.) was evaluated by mixing both in a 1:1 by weight ratio. Mixtures were pelletized and heated at 1173 K for 15 h under air to simulate the electrode preparation conditions. Phase analysis was then performed by XRD.

The area-specific resistances (ASR) associated to the total electrochemical processes at the electrodes have been determined from impedance diagrams at different temperatures in air on symmetrical two-electrode configuration cells as described previously.[6] Electrolyte pellets of commercial CGO were prepared by pressing the powder at 250 MPa and sintering in air at 1673 K for 12 hours (heating/cooling rate of 2.5 K min^{-1}) to obtain discs of relative densities higher than 97% of 10 mm diameter and 1 mm thickness. Slurries were prepared by mixing $Sr_2CoNb_xTi_{1-x}O_{6-\delta}$ (0≤x≤1) and commercial CGO composite (70:30 wt %) with Decoflux^{TM} (WB41, Zschimmer and Schwarz) as a binder, and deposited onto both sides of the electrolyte pellet. Finally, the symmetric cells were fired at 1173 K for 3 h in air (heating/cooling rate of 2.5 K min–1). Silver paste and silver mesh were used as current collectors. The measurements were carried out in air on heating and cooling cycles between 773 and 973 K using a frequency response analyzer and a dielectric interface (Solartron 1255 and 1296, respectively) in the frequency range 0.1 Hz to 1 MHz with an excitation voltage of 50 mV. The ASR values have been determined from impedance spectra by fitting to equivalent circuits model and corrected considering the electrode surface area and the symmetrical configuration[25] using ZView software.[36]

Associated Content

Figure SI 1 shows the back-scattered electron (BSE) image of the x=0.3 of the series, $Sr_2CoNb_{0.7}Ti_{0.3}O_{6-\delta}$, together with the corresponding element-distribution maps. Figure SI 2. Back-scattered electron (BSE) image of $Sr_2CoNb_{0.5}Ti_{0.5}O_{6-\delta}$. Figure SI 3. Back-scattered electron (BSE) image of $Sr_2CoNb_{0.1}Ti_{0.9}O_{6-\delta}$. Figure SI 4. Experimental and calculated

FULL PAPER

XRD patterns for $Sr_2CoNbO_{6-\delta}$. Figure SI 5. Experimental and calculated XRD patterns for $Sr_2CoNb_{0.90}Ti_{0.10}O_{6-\delta}$. Figure SI 6. Experimental and calculated XRD patterns for $Sr_2CoNb_{0.80}Ti_{0.20}O_{6-\delta}$. Figure SI 7. Experimental and calculated XRD patterns for $Sr_2CoNb_{0.70}Ti_{0.30}O_{6-\delta}$. Figure SI 8. Experimental and calculated XRD patterns for $Sr_2CoNb_{0.50}Ti_{0.50}O_{6-\delta}$. Figure SI 9. Experimental and calculated XRD patterns for $Sr_2CoNb_{0.40}Ti_{0.60}O_{6-\delta}$. Figure SI 10. Experimental and calculated XRD patterns for $Sr_2CoNb_{0.30}Ti_{0.70}O_{6-\delta}$. Figure SI 11. Experimental and calculated XRD patterns for $Sr_2CoNb_{0.20}Ti_{0.80}O_{6-\delta}$. Figure SI 12. Experimental and calculated XRD patterns for $Sr_2CoNb_{0.10}Ti_{0.90}O_{6-\delta}$. Figure SI 13. Experimental and calculated XRD patterns for Sr_2CoTiO_6. Figure SI 14. Thermal evolution under dynamical vacuum of the cell parameters for the x=0.9 member of the series $Sr_2CoNb_{1-x}Ti_xO_{6-\delta}$. Figure SI 15. Thermal evolution under dynamical vacuum of the cell parameters for the x=0.1 member of the series $Sr_2CoNb_{1-x}Ti_xO_{6-\delta}$. Oxides $Sr_2CoNb_{1-x}Ti_xO_{6-\delta}$ with low Ti-content ($0 \leq x \leq 0.2$) are unstable under reducing conditions (firing 1173 K for 24 h under a continuous 5% H_2/Ar gas mixture stream). Segregations of small particles (around 250 nm diameter) at the grain boundaries are observed in Fig. SI 16. The element distribution maps shown in Fig. SI 17, reveal that those particles mainly contain cobalt. Figure SI 16. Back-scattered electron (BSE) image of a reduced pellet of $Sr_2CoNbO_{6-\delta}$. Figure SI 17. (a) Back-scattered electrons (BSE) image taken at a magnification of x4000 and element distribution maps of a reduced $Sr_2CoNbO_{6-\delta}$ sample: (b) Sr, (c) Nb, (d) Co and (e) O. Segregation of Co-rich particles is indicated on (a) and (d). Figure SI 18. XAS measurements on the pristine and a reduced sample of $Sr_2CoNb_{0.1}Ti_{0.9}O_{6-\delta}$ (a) XANES spectra with corresponding references of Co and (b) module of the Fourier transform of the EXAFS spectra of pristine and reduced $Sr_2CoNb_{0.1}Ti_{0.9}O_{6-\delta}$. Figure SI 19: XRD pattern of a) $Sr_2CoNb0.70Ti0.30O6$/YSZ and b) $Sr_2CoNb_{0.70}Ti_{0.30}O_{6-\delta}$/CGO mixtures (1:1) after heated in air at 1173 K for 15 hours. Table SI 1. Refined parameters of equivalent circuits used to fit IS spectra for $Sr_2CoTiO_{6-\delta}$ at different temperatures on heating, capacitance and relaxation frequency are also given. Table SI 2. Refined parameters of equivalent circuits used to fit IS spectra for $Sr_2CoTiO_{6-\delta}$ at different temperatures on cooling after heating at 973 K, capacitance and relaxation frequency are also given. Table SI 3. Refined parameters of equivalent circuits used to fit IS spectra for $Sr_2CoTiO_{6-\delta}$ at different temperatures on heating, capacitance and relaxation frequency are also given. Table SI 4. Refined parameters of equivalent circuits used to fit IS spectra for $Sr_2CoTiO_{6-\delta}$ at different temperatures on cooling after heating at 973 K, capacitance and relaxation frequency are also given.

Entry for the Table of Contents (Please choose one layout)

Layout 1:

FULL PAPER

Text for Table of Contents
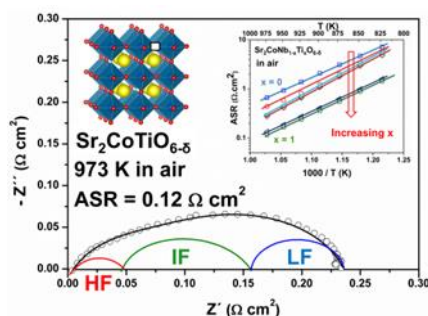
Author(s), Corresponding Author(s)*

Page No. – Page No.

Title

[1]   aL. Zhu, R. Ran, M. Tadé, W. Wang, Z. Shao, *Asia-Pacific Journal of Chemical Engineering* **2016**, *11*, 338-369; bA. Jun, J. Kim, J. Shin, G. Kim, *ChemElectroChem* **2016**, *3*, 511-530; cS. J. Skinner, *Fuel Cells Bulletin* **2001**, *4*, 6-12.

[2]   aS. W. Tao, J. T. S. Irvine, *Advanced Materials* **2006**, *18*, 1581-1584; bY. Gan, J. Zhang, Y. Li, S. Li, K. Xie, J. T. S. Irvine, *Journal of The Electrochemical Society* **2012**, *159*, F763-F767.

[3]   J. Sunarso, S. Baumann, J. M. Serra, W. A. Meulenberg, S. Liu, Y. S. Lin, J. C. Diniz da Costa, *Journal of Membrane Science* **2008**, *320*, 13-41.

[4]   aK. Huang, M. Feng, J. B. Goodenough, M. Schmerling, *Journal of The Electrochemical Society* **1996**, *143*, 3630-3636; bK. Huang, H. Y. Lee, J. B. Goodenough, *Journal of The Electrochemical Society* **1998**, *145*, 3220-3227.

[5]   M. T. Azcondo, J. Romero de Paz, K. Boulahya, C. Ritter, F. Garcia-Alvarado, U. Amador, *Dalton Transactions* **2015**, *44*, 3801-3810.

[6]   J. C. Ruiz-Morales, J. Canales-Vázquez, J. Peña-Martínez, D. M. López, P. Núñez, *Electrochimica Acta* **2006**, *52*, 278-284.

[7]   M. Yuste, J. C. Perez-Flores, J. R. de Paz, M. T. Azcondo, F. Garcia-Alvarado, U. Amador, *Dalton Transactions* **2011**, *40*, 7908-7915.

[8]   A. Gomez-Perez, M. T. Azcondo, M. Yuste, J. C. Perez-Flores, N. Bonanos, F. Porcher, A. Munoz-Noval, M. Hoelzel, F. Garcia-Alvarado, U. Amador, *Journal of Materials Chemistry A* **2016**, *4*, 3386-3397.

[9]   aG. J. Wang, C. C. Wang, S. G. Huang, X. H. Sun, C. M. Lei, T. Li, L. N. Liu, *AIP Advances* **2013**, *3*, 022109; bJ. Bashir, R. Shaheen, *Solid State Sciences* **2011**, *13*, 993-999.

[10]   G. Blasse, *Journal of Applied Physics* **1965**, *36*, 879-883.

[11]   aK. Szot, W. Speier, G. Bihlmayer, R. Waser, *Nat Mater* **2006**, *5*, 312-320; bS. F. Shao, J. L. Zhang, P. Zheng, W. L. Zhong, C. L. Wang, *Journal of Applied Physics* **2006**, *99*, 084106; cA. Kalabukhov, R. Gunnarsson, J. Börjesson, E. Olsson, T. Claeson, D. Winkler, *Physical Review B* **2007**, *75*, 121404.

[12]   F. Prado, A. Manthiram, *Journal of Solid State Chemistry* **2001**, *158*, 307-314.

[13]   H. Hayashi, M. Kanoh, C. J. Quan, H. Inaba, S. Wang, M. Dokiya, H. Tagawa, *Solid State Ionics* **2000**, *132*, 227-233.

[14]   P. S. Napolsky, O. A. Drozhzhin, S. Y. Istomin, S. M. Kazakov, E. V. Antipov, A. V. Galeeva, A. A. Gippius, G. Svensson, A. M. Abakumov, G. Van Tendeloo, *Journal of Solid State Chemistry* **2012**, *192*, 186-194.

[15]   V. Kunzl, *Collect. Trav. Chim. Techecolovaquie* **1932**, *4*.

[16]   F. E. Sowrey, L. J. Skipper, D. M. Pickup, K. O. Drake, Z. Lin, M. E. Smith, R. J. Newport, *Physical Chemistry Chemical Physics* **2004**, *6*, 188-192.

[17]   T. Yamamoto, *X-Ray Spectrometry* **2008**, *37*, 572-584.

[18]   aD. Carlier, J.-H. Cheng, C.-J. Pan, M. Ménétrier, C. Delmas, B.-J. Hwang, *The Journal of Physical Chemistry C* **2013**, *117*, 26493-26500; bM. Hunault, J. L. Robert, M. Newville, L. Galoisy, G. Calas, *Spectrochimica Acta Part A: Molecular and Biomolecular Spectroscopy* **2014**, *117*, 406-412.

[19]   B. Raveau, Seikh, M. , *Cobalt Oxides: From Crystal Chemistry to Physics*, Wiley-VCH, Berlin, **2012**.

[20]   J. M. Rendon-Ramirez, O. A. Almanza, R. Cardona, D. A. Landinez-Tellez, J. Roa-Rojas, *International Journal of Modern Physics B* **2013**, *27*, 1350171-1350182.

[21]   A. Staykov, H. Tellez, T. Akbay, J. Druce, T. Ishihara, J. Kilner, *Chemistry of Materials* **2015**, *27*, 8273-8281.

[22]   aS. Xu, X. Lin, B. Ge, D. Ai, Z. Peng, *Journal of the Ceramic Society of Japan* **2016**, *124*, 813-818; bK. Yoshi, *J. Alloys and Compd.* **2000**, *307*, 119.

[23]   F. Wang, Q. Zhou, T. He, G. Li, H. Ding, *Journal of Power Sources* **2010**, *195*, 3772-3778.

[24]   T. Xia, J. Wang, N. Lin, H. Zhao, L. Huo, X. Cao, J. Meng, *ECS Transactions* **2008**, *13*, 207-215.

[25]   aS. B. Adler, *Solid State Ionics* **1998**, *111*, 125-134; bS. B. Adler, *Chem. Rev* **2004**, *104*, 4791-4844.

[26]   A. Flura, C. Nicollet, S. Fourcade, V. Vibhu, A. Rougier, J. M. Bassat, J. C. Grenier, *Electrochimica Acta* **2015**, *174*, 1030-1040.

[27]   M. J. Escudero, A. Aguadero, J. A. Alonso, L. Daza, *Journal of Electroanalytical Chemistry* **2007**, *611*, 107-116.

[28]   M. González-Cuenca, W. Zipprich, B. A. Boukamp, G. Pudmich, F. Tietz, *Fuel Cells* **2001**, *1*, 256-264.

[29]   P. Hjalmarsson, M. Søgaard, M. Mogensen, *Solid State Ionics* **2009**, *180*, 1395-1405.

[30]   K. Boulahya, D. Munoz Gil, M. Hassan, S. Garcia Martin, U. Amador, *Dalton Transactions* **2017**.

[31]   G. Amow, J. Au, I. Davidson, *Solid State Ionics* **2006**, *177*, 1837-1841.

[32]   K. W. Song, K. T. Lee, *Ceramics International* **2011**, *37*, 573-577.

[33]   J. Rodríguez-Carvajal, *Physica B: Condensed Matter* **1993**, *192*, 55-69. The program and manual can be found at http://www.ill.eu/sites/fullprof/.
[34]   B. Ravel, M. Newville, *Journal of Synchrotron Radiation* **2005**, *12*, 537-541.
[35]   A. L. Ankudinov, B. Ravel, J. J. Rehr, S. D. Conradson, *Physical Review B* **1998**, *58*, 7565-7576.
[36]   D. Johnson, *ZView: A software Program for IES Analy* **2005**.